Available online at www.sciencedirect.com
ScienceDirect
Journal of the European Ceramic Society 31 (2011) 97–109
www.elsevier.com/locate/jeurceramsoc

High resolution optical microprobe investigation of surface grinding stresses in Al_2O_3 and Al_2O_3/SiC nanocomposites

Sheng Guo [1], Apichart Limpichaipanit [2], R.I. Todd *

University of Oxford, Department of Materials, Parks Road, Oxford OX1 3PH, United Kingdom

Received 26 April 2010; received in revised form 8 June 2010; accepted 23 August 2010

Abstract

It has previously been suggested that Al_2O_3/SiC nanocomposites develop higher surface residual stresses than Al_2O_3 on grinding and polishing. In this work, high spatial resolution measurements of residual stresses in ground surfaces of alumina and nanocomposites were made by Cr^{3+} fluorescence microspectroscopy. The residual stresses from grinding were highly inhomogeneous in alumina and 2 vol.% SiC nanocomposites, with stresses ranging from ~ -2 GPa within the plastically deformed surface layers to $\sim +0.8$ GPa in the material beneath them. Out of plane tensile stresses were also present. The stresses were much more uniform in 5 and 10 vol% SiC nanocomposites; no significant tensile stresses were present and the compressive stresses in the surface were ~ -2.7 GPa. The depth and extent of plastic deformation were similar in all the materials (depth $\sim$ 0.7–0.85 μm); the greater uniformity and compressive stress in the nanocomposites with 5 and 10 vol% SiC was primarily a consequence of the lack of surface fracture and pullout during grinding. The results help to explain the improved strength and resistance to severe wear of the nanocomposites.

Keywords: Al_2O_3; Nanocomposites; Residual stresses; Spectroscopy; Fluorescence microscopy

1. Introduction

Al_2O_3/SiC nanocomposites combine polycrystalline alumina and small amounts of sub-micron SiC particles [1–3]. The typical microstructure of Al_2O_3/SiC nanocomposites is composed of a polycrystalline matrix with an average size of 1–5 μm and SiC particles with size ranging from 100 to 200 nm. The addition of a small amount of sub-micron sized SiC to the alumina matrix can significantly improve the surface finish after machining, the resistance to severe wear, and the strength [1–11]. The nanocomposites have better surface finish and wear resistance both because the mean size of the individual pieces of material removed by brittle fracture at the surface is reduced and because the initiation of fracture is itself suppressed by the SiC additions [12,13]. The strengthening mechanism of nanocomposites, however, is still controversial and a number of possible mechanisms have been proposed. One obvious explanation is simply the improved surface finish and reduction in cracking during specimen preparation mentioned above. Another related suggestion is that the compressive surface residual stress after machining is increased [9,14,15]. In this work, the grinding induced surface residual stresses in Al_2O_3 and Al_2O_3/SiC nanocomposites are measured and compared, in order to investigate the validity of the proposed residual stress strengthening mechanism.

Previously, grinding induced surface residual stresses in Al_2O_3 and Al_2O_3/SiC materials have been measured by X-ray diffraction [14,16,17], curvature measurement [15] and Hertzian indentation [18,19]. The disadvantage of these techniques is that they all have poor spatial resolution compared with the scale of the microstructure [20] and as a result the measured stress is volume averaged rather than reflecting the local stress at the surface and its spatial distribution. Furthermore, the mean stress deduced depends on estimating a thickness for the compressive surface layer and often there is little information about what value this should take.

* Corresponding author. Tel.: +44 1865 273718; fax: +44 1865 273783.
E-mail addresses: mmsguo@polyu.edu.hk (S. Guo), apilim@chiangmai.ac.th (A. Limpichaipanit), richard.todd@materials.ox.ac.uk (R.I. Todd).
[1] Department of Mechanical Engineering, The Hong Kong Polytechnic University, Hung Hom, Kowloon, Hong Kong.
[2] Department of Physics and Materials Science, Faculty of Science, Chiang Mai University, Chiang Mai 50200, Thailand.

0955-2219/$ – see front matter © 2010 Elsevier Ltd. All rights reserved.
doi:10.1016/j.jeurceramsoc.2010.08.021

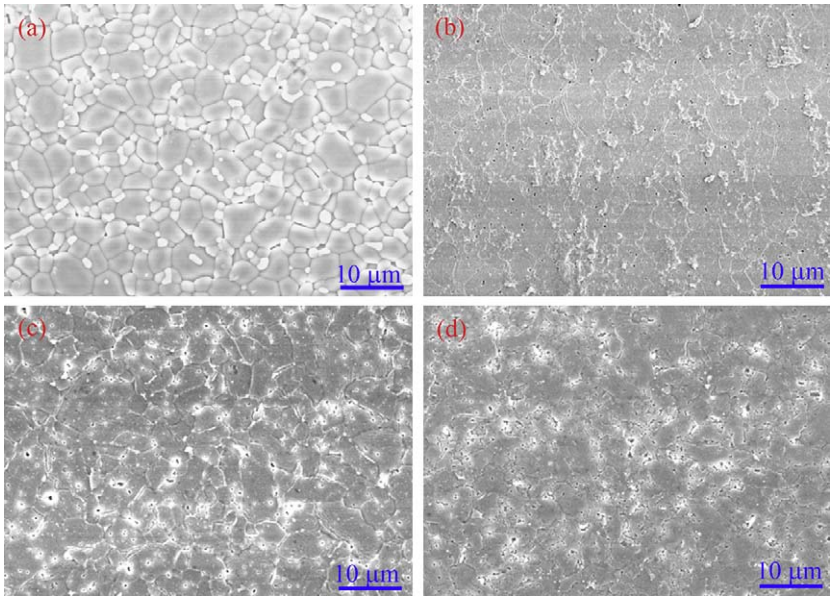

Fig. 1. Microstructure of the Al_2O_3 and Al_2O_3/SiC nanocomposites used in this work. (a) Al_2O_3, (b) 2 vol.% SiC, (c) 5 vol.% SiC and (d) 10 vol.% SiC. The specimens were thermally etched at 50 °C below the sintering temperature for 30 min in vacuum to reveal the grain boundaries.

To probe the local stress variation in the ground surfaces more directly, a higher spatial resolution technique is required. In this work, confocal Cr^{3+} fluorescence microscopy was used, with lateral and axial (depth) resolutions of ~1.5 μm and ~3 μm, respectively [21,22]. Previous work on alumina based materials using Cr^{3+} fluorescence microscopy investigated only residual stresses induced by indentation or scratching [23,24]; in addition, it used weakly confocal microscopes with depth resolution of ~10 μm. From both TEM observations [18] and results in our previous work [25], it is known that grinding stresses are expected to be found at depths of ~1 μm for monolithic alumina. Considering the translucency of alumina materials, therefore, the conclusion in Ref. [24] that the residual stresses around indentations and scratches in alumina were lower than in alumina/SiC nanocomposites may be an artefact of lower transparency in the nanocomposites, which would confine the sampled volume more closely to the stressed region.

The confocal microscope used in this work alleviates this problem but does not entirely remove it because the axial resolution is still not sufficient to make simple point measurements of surface stress. The experimentally measured stress is actually the convolution of the real stress with the axial probe response function (PRF) [26] which describes the relative collection efficiency as a function of depth and depends on the instrument and the translucency of the material. In our previous work, on ground surfaces of alumina, residual stress distributions were estimated by modelling the plastic displacement of material resulting from grinding as an array of continuously distributed edge dislocations [21,25], and established the PRF of our instrument when used with Al_2O_3 and Al_2O_3/SiC [21,22]. The convolution of the fluorescence response predicted by the model with the PRF allowed the local residual stress variation for polycrystalline alumina after grinding and polishing to be estimated by adjusting the physical parameters in the model to fit the experimental results. In the current work, the same method will be used to compare the local stress distributions in surface ground monolithic Al_2O_3 and Al_2O_3/SiC nanocomposites.

2. Experimental

2.1. Materials and specimen preparation

The starting powders were AKP50 alumina (200 nm, Sumitomo, Japan, 99.995% purity) and UF45 SiC (260 nm, Lonza, Germany, contains 0.2% free Si, 0.6% free C and 3.5% oxygen) respectively. 0.25 wt% MgO was added to all materials to prevent abnormal grain growth. Mechanical mixing by attrition milling (Szegvari HD, USA) using yttria stabilized zirconia milling media was performed at a speed of 300 rpm for 2 h. The ratio of water to powder was 4:1 by volume and 2.1 wt.% of Dispex A40 (Allied Colloids, UK) was used as a dispersant. The mixture was freeze dried (Edwards Micromodulyo, UK) for 24 h. The powder was passed through a 150 μm sieve and then calcined at 600 °C for 1 h. Hot pressing was used to produce dense specimens. A pressure of 25 MPa was applied for 30 min in an argon atmosphere with a graphite die at maximum temperatures between 1550 and 1700 °C, to give materials of similar grain size (5–6 μm (Fig. 1), measured by the conventional liner intercept method [27]). Three Al_2O_3/x vol.% SiC nanocomposite (x = 2, 5, 10) specimens were used in this work, and a monolithic alumina specimen was used as a comparison. The grain sizes of the materials are given in Table 1.

2.2. Grinding

The procedure for grinding of the specimens followed our previous work [25]. Specimens were sequentially polished down to a 1 μm diamond finish first to start from smooth surfaces, and they were then ground on a resin bonded alumina wheel for

Table 1
List of average grain size of Al_2O_3 and Al_2O_3/SiC nanocomposites, and their pullout size and fraction of pullout after grinding.

Materials	Average grain size (μm)	Mean pullout size (μm)	Area fraction of pullout (%)
Al_2O_3	5.6	5.5	60 ± 7
2 vol.% SiC	6.2	4.1	50 ± 1
5 vol.% SiC	5.3	1.9	3 ± 1
10 vol.% SiC	4.9	1.7	1.2 ± 0.4

4 min using 45 μm grit diamond spray. The appearance of the ground surfaces, especially for monolithic alumina and 2 vol.% SiC nanocomposite, consisted of two distinctive features (Fig. 2) [12]: (i) "ground" regions, which are relatively flat and which, when examined in the scanning electron microscope (SEM), show scratches produced by plastic deformation of the surface [12] and (ii) "pullouts", where a piece of material has been removed from the surface by brittle fracture around its periphery. The term "pullout" in this work refers to the cavity left in the surface of the bulk specimen when a piece of material is removed, rather than the removed piece itself. The mean equivalent circular diameter of the individual surface pullouts and the area fraction of pullout were measured from the scanning electron microscopy (SEM) micrographs following the procedure described elsewhere [12,13] and is given in Table 1.

2.3. Cr^{3+} fluorescence measurements

The principle of Cr^{3+} fluorescence microscopy is to measure the stress-induced shifts of the characteristic spectral lines associated with Cr^{3+} substitutional impurities in alumina (the R1 and R2 lines, with typical wavenumbers of 14,402 and 14,432 cm^{-1}, respectively). The shift can be related to stress through the piezospectroscopic (PS) coefficients [23,28–32]:

$$\Delta\nu = \Pi_{ij}\sigma_{ij} \quad (1)$$

where $\Delta\nu$ is the peak shift (cm^{-1}), σ_{ij} are the stress components (GPa) and Π_{ij} are the PS coefficients (cm^{-1} GPa^{-1}), defined in the crystallographic axial system. The PS coefficients for alumina are positive, so from Eq. (1) it is seen that a positive peak shift indicates the presence of tensile stresses, while a negative peak shift corresponds to compressive stresses.

The fluorescence microscopy experiments were performed using a confocal Raman microscope (System 1000, Renishaw, UK) and incident radiation from a He–Ne laser at 633 nm. Although the alumina powder used to make the specimens had a purity of at least 99.995% according to the manufacturer, the specimens contained enough Cr^{3+} to give strong spectral peaks without the need to add more artificially. A 100 × /0.9NA lens was used. The confocal aperture in the instrument is formed by the intersection of two slits at 90° to one another. One is a physical slit, which in the experiments described here was set to 10 μm. The other slit is virtual and is formed using only a narrow stripe of pixels in the CCD camera that collects the diffraction pattern from the grating used to analyse the luminescent spectrum. The width of this stripe was set to 2 pixels in our experiments, which gives a virtual slit width similar to the 10 μm width of the real slit at 90° to it.

In order to measure the residual stresses, depth scans were performed through the ground surfaces of the specimens [21,22,25]. Each scan was made through the approximate centre of either a "ground" region or a "pullout" (see Section 2.2). The laser was initially focused on the local sample surface at the beginning and the position of the focal plane relative to the surface at this point was defined as $z = 0$. The specimen was then moved with the motorized microscope stage so that the focus point scanned from above to below the sample surface. The dis-

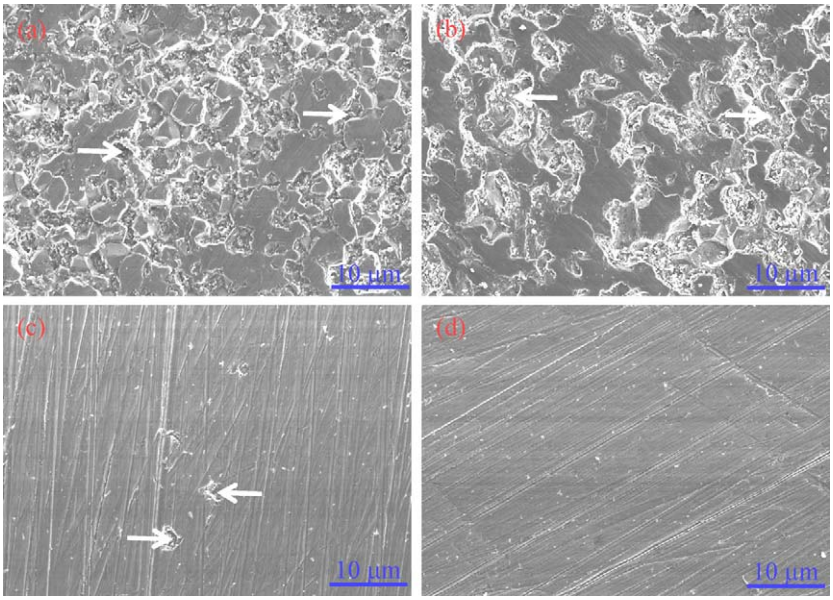

Fig. 2. SEM images of ground surfaces of Al_2O_3 and Al_2O_3/SiC nanocomposites. (a) Al_2O_3, (b) 2 vol.% SiC, (c) 5 vol.% SiC and (d) 10 vol.% SiC. The arrows in the image indicate the "pullout" regions.

placement of the sample surface relative to the focal plane, Δz, is defined to be positive as the optical probe moves into the specimen, away from the surface. The step size was 1 μm for the nanocomposites and 2 μm for monolithic alumina with an exposure time of 20 s per point. The peak position and intensity were determined in most cases by fitting both R1 and R2 peaks using the mixed Lorentzian and Gaussian function using a commercial package, Grams/32 (Galactic Industries, USA). This procedure will be termed *two-peak fitting* in what follows. Some spectra collected with the optical probe focused very close to the "ground" regions of surface ($\Delta z \sim \pm 2$ μm), could not be fitted well using two-peak fitting [21,25]; instead, an extra doublet of R1 and R2 peaks was required to give a good fit (termed *four-peak fitting*). The four-peak fitting was carried out using an alternative fitting programme, Auto2Fit (7-D Software, China) and was done subject to the constraint that the R1 to R2 peak area ratio was 2.0 for each of the two fitted doublets. This is discussed further in Section 3.3 and Refs. [21,25].

The R1 peak position was used to characterize the peak shift, $\Delta\nu$, and the reference positions were determined from the average R1 positions (spectra collected on 20 random points) on the 1 μm grit polished surface of individual specimens, assumed to be residual stress free.

3. Results

3.1. Microstructure observation after grinding

SEM micrographs for the ground surfaces of monolithic alumina and Al_2O_3/x vol.% SiC ($x = 2$, 5, 10) nanocomposites are shown in Fig. 2. From the micrographs, it is observed that:

(1) 5 and 10 vol.% SiC nanocomposites have much better surface finish after grinding compared to those of monolithic alumina and 2 vol.% SiC nanocomposite. This can be attributed to the decrease of pullout size and also the suppression of pullout formation [9,12]. The pullout size decreases as the amount of SiC increases (Table 1). Ortiz Merino and Todd [12,33] used a simple geometrical model to explain this as the result of the fracture mode transition from intergranular fracture in the monolithic alumina to transgranular fracture in the nanocomposites. The 5 and 10 vol.% SiC nanocomposites also have a much smaller area fraction of pullouts compared to those of monolithic alumina and 2 vol.% SiC nanocomposite (Table 1), which is possibly due to the large amount of nano-sized SiC addition blocking the formation of long twins and dislocation pileups that are responsible for crack initiation [33].

(2) For monolithic alumina, much of the material removal is by grain dislodgement through intergranular fracture; when 2 vol.% SiC is added, the dominant fracture mode changes to transgranular; when more than 5 vol.% SiC is added, plastic deformation (ploughing), instead of brittle fracture, becomes the main material removal mechanism which is reflected by the grooves seen in Fig. 2(c) and (d). These observations of the surface appearance are in agreement with previous reports [12,18,34].

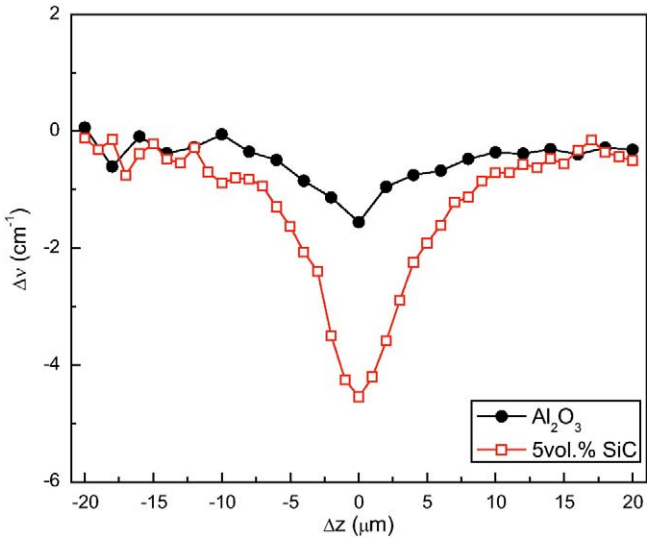

Fig. 3. Depth profiles through the pullout region for alumina and 5 vol.% SiC nanocomposite.

3.2. Depth scans in "pullout" regions

The nominal residual stresses in ground Al_2O_3 and Al_2O_3/SiC nanocomposites were assessed qualitatively by the depth scan method used previously for polycrystalline aluminas subjected to grinding and polishing treatments [25].

Typical depth profiles (i.e., $\Delta\nu$ for the R1 peak vs. Δz curves) centred on "pullout" regions are given in Fig. 3. $\Delta z = 0$ here is defined to be the surface at the bottom of each pullout, where the laser was initially focused (see Section 2.3). The curves for both the alumina and the nanocomposite exhibit a clear minimum as the optical probe passes through the surface, indicating the presence of compressive residual stresses. However, the extent of the negative peak shift is significantly greater for the nanocomposite. The reasons for this will be discussed in Section 4.

Examination of many such regions showed that the precise extent of the peak shifts varied between individual pullouts. This scatter due to variations in the local environment was also seen in the depth scan results from "ground" regions of the surface [21,25]. For simplicity, only results with intermediate peak shifts are shown in the following sections but the conclusions drawn are representative of the wider range of results. The level of uncertainty in stress arising from this consideration is discussed in Section 3.4.

3.3. Depth scans in "ground" regions

Excellent fitting was obtained using two peaks for all pullout results and for most of the spectra obtained from the "ground" regions, as seen in the inset in Fig. 4(a). However, careful examination showed that spectra collected with the optical probe focused at or close to the surface in ground regions could not be fitted well using the two-peak fitting procedure, as exemplified in Fig. 4(a). This fitting problem has been discussed in detail in our previous work [21,25] and the solution is shown in Fig. 4(b). Another pair of R1 and R2 peaks is added to give a good fit and

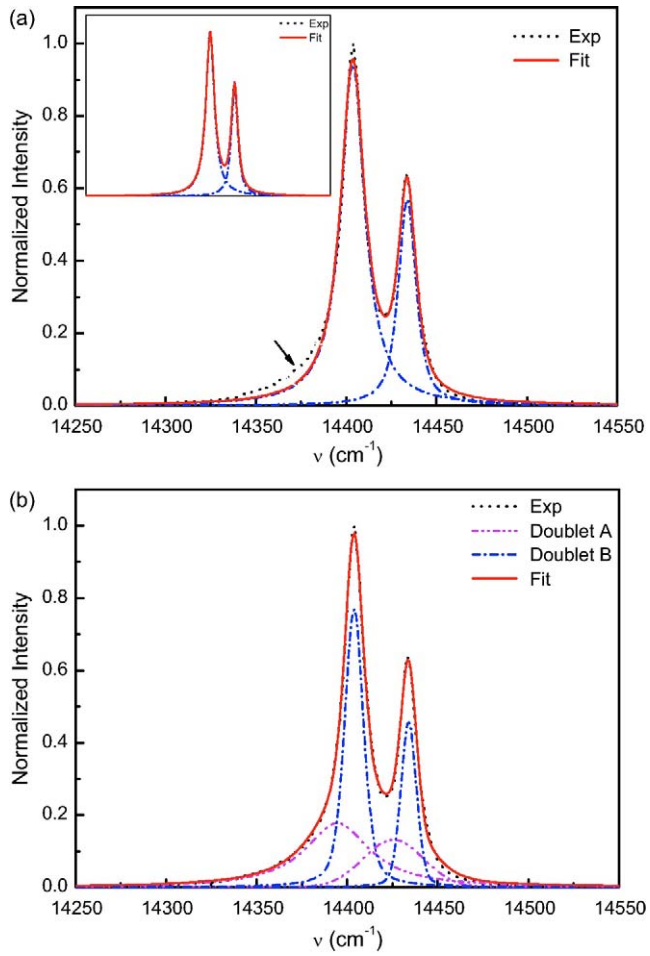

Fig. 4. (a) An example of the misfit using the two-peak fitting to fit a spectrum collected from near the ground surface, with the arrow indicating the misfit. The inset shows that two-peak fitting works well for spectra collected far away from the ground surface. (b) Improvement of curve fitting in (a) by using four-peak fitting.

a fitting constraint for peak area (intensity) ratio of R1 to R2 is applied to both doublets (=2.0) to make the fitting parameters physically meaningful [21,31,35]. It is argued that the two distinct doublets have a physical interpretation [21,25] in that one represents the stress state within the *plastically* deformed layer at the surface in the ground regions and the other represents the stress state in the *elastically* deformed material below it. Both volumes are, however, sampled simultaneously due to the low axial resolution of the instrument [21,22] relative to the thickness of the plastically deformed layer [21,25]. Using four-peak fitting, the two stress states can be distinguished by identifying each with one of the fitted doublets, *provided* that the peak shape is sufficiently distinctive and the fitting routine sufficiently robust to separate these doublets correctly. Grounds for believing that these criteria are satisfied in this work rely on the fact that one of the doublets is shifted significantly relative to other, as will be seen below. There are two main pieces of evidence that this separation is physically meaningful in our results. First, similar results are obtained for the weaker doublet from different "ground" regions within the same sample, indicating that this second doublet is not an arbitrary mathematically generated artefact that improves the fit simply by introducing more adjustable parameters. Secondly, the shifts of the severely overlapping R2 peaks for each doublet give remarkably similar conclusions regarding the stresses to those deduced using the better defined R1 peaks, again supporting the physical interpretation of the results.

In accordance with the terminology we used in our previous work [25], the R1 peaks representing the stress states within the plastically deformed layer will be called *broad peaks* (broadening comes from the wide range of stresses induced by dislocations and twins [18]) and the R1 peaks representing the stress states in the elastically deformed material below it will be termed *sharp peaks*.

Fig. 5(a) shows typical shifts of the broad peak relative to the reference value as a function of Δz for Al_2O_3 and the 5 vol.% Al_2O_3/SiC nanocomposite. Only two spectra needed the four-peak fitting for Al_2O_3 and three for the 5 vol.% SiC nanocomposite in the cases shown. Both results show large neg-

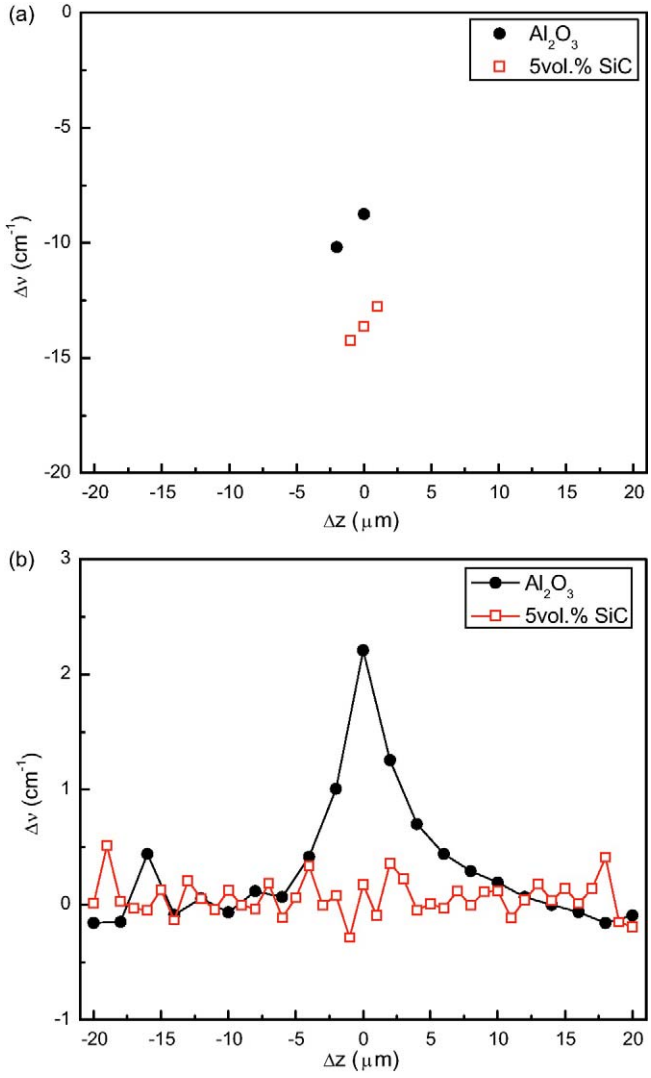

Fig. 5. Separated broad peak shifts (a) and sharp peak shifts (b) from the depth profile through the ground surface of alumina and 5 vol.% SiC nanocomposite analysed using four-peak fitting where necessary.

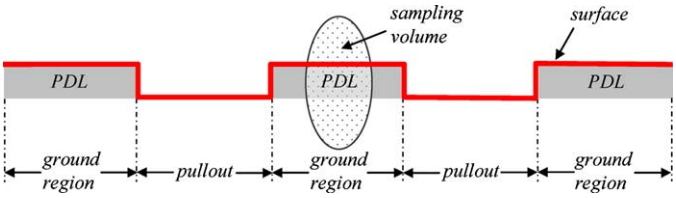

Fig. 6. Schematic of the sampling volume of the microscope during a depth scan through a ground region and the surface residual stress. PDL denotes plastically deformed layers, assumed to be under compression. The broad fluorescence peaks are taken to come from the intersection of the sampling volume with the PDL and the sharp peaks from the part of the sampling volume below the PDL.

ative peak shifts, with average values of $\sim -9.5\,\mathrm{cm}^{-1}$ and $\sim -13.5\,\mathrm{cm}^{-1}$, respectively. The source of the small variation of the broad peak shift with Δz is probably the uncertainty in the fitting [25] and the average peak shift of the broad peak has been used to fit the model predictions below (Section A.3). These large negative peak shifts indicate highly compressive stresses, as expected in the plastically deformed surface layer.

Typical sharp-peak shifts as a function of Δz for Al_2O_3 and 5 vol.% Al_2O_3/SiC nanocomposite are shown in Fig. 5(b), where most of the peak positions are fitted using two-peak fitting (the results are from the same depth scan as for Fig. 5(a), so the points for which four peak fitting was necessary can easily be identified). No obvious discontinuity is evident in the points obtained from four-peak fitting. A distinct maximum relative to the reference position ($\Delta v = 0$) is found in the sharp peak results for Al_2O_3 and the 2 vol.% SiC nanocomposite, but no significant shift was seen for the 5 and 10 vol.% SiC nanocomposites (results for 2 and 10 vol.% SiC nanocomposites not shown here). This means the mean stress immediately beneath the assumed compressive surface layer is tensile in Al_2O_3 and the 2 vol.% SiC nanocomposite, but nearly zero in the 5 and 10 vol.% SiC nanocomposites.

The results given above show that the surface stresses in ground surfaces are highly inhomogeneous, and differ significantly between Al_2O_3 and Al_2O_3/SiC nanocomposites. Tensile stresses are present in some regions in alumina and 2 vol.% SiC nanocomposite, but not in 5 and 10 vol.% SiC nanocomposites; strongly compressive stresses are present in other regions, as indicated previously by those techniques that only measure the mean stresses [9,14,15]. However, these conclusions are essentially qualitative; a quantitative understanding of these stresses needs more sophisticated analysis.

3.4. Quantitative interpretation of the experiment results

To interpret the experimental results quantitatively, we assume that the sampling volume of the microscope during a depth scan through a ground region can be schematically represented by Fig. 6 [25]. Our approach is (1) to develop an elastic model for the near-surface stresses, (2) to describe the sampling volume of the fluorescence microscope using its axial PRF, then (3) to convolute the peak shift predicted by the stress model with the PRF, adjusting the physical parameters in the model to obtain good agreement with the experimental depth scan results. A quantitative estimate of the stresses and their distribution can then be extracted from the model. This approach has been applied to resolve the residual stresses in ground and polished polycrystalline aluminas in our previous work [25], and is summarised in the Appendix of this paper.

Table 2
List of D', d, s and p for Al_2O_3 and Al_2O_3/SiC nanocomposites. D' and d are from the best fit of the model to the experimental results; s and p are measured directly from SEM images.

Materials	D' (GPa)	d (μm)	$D'\cdot d$ (GPa μm)	s (μm)	p (μm)	s/p
Al_2O_3	0.37	0.71	0.26	3.7	5.5	0.67
2 vol.% SiC	0.25	0.80	0.2	4.1	4.1	1
5 vol.% SiC	0.34	0.82	0.28	61.4	1.9	32.3
10 vol.% SiC	0.36	0.85	0.31	142.4	1.7	83.8

Fig. 7 shows typical comparisons between experiment and the optimised model for scans through the specimen surfaces. The agreement between the model and the experimental results is quite reasonable considering the idealised nature of the model. Notably, the model successfully captures the presence of tensile stresses in the "sharp" peak results representing the material beneath the ground regions of surface in alumina and the 2 vol.% SiC nanocomposite, and the absence of such stresses in the 5 and 10 vol.% SiC nanocomposites (results for 2 and 10 vol.% SiC nanocomposites not shown here). The less satisfactory fitting at a greater depth is a consequence of the collected signal coming from to the extreme tail of the PRF, which is not accurately described by the mathematical PRF function used [21].

In the stress model (Section A.1), there are four parameters characterising the surface deformation and fracture responsible for the residual stresses, namely s, p, D' and d. s and p are the breadths for the islands of ground surface and the pullouts, respectively, as indicated in Fig. A1. s and p can be determined experimentally as p can be regarded as the mean pullout diameter and s can be calculated from the area fraction of pullout: as the stress model is based on a simplified two dimensional condition, the pullout fraction $= p/(p+s)$. D' characterises the severity of plastic deformation in the plastically deformed layer and d represents the depth of this plastically deformed layer. D' and d are determined from the best fit of the model to the experimental results. The values of the experimentally determined s and p, together with the fitted D' and d for Al_2O_3 and Al_2O_3/SiC nanocomposites are listed in Table 2. D' and d are similar for the Al_2O_3 and Al_2O_3/SiC nanocomposites (Fig. 8), considering the accuracy of the fitting parameters. The typical scatter for D' and d is within 20% and 35% [25], respectively, based on their values determined from various depth scan results made at different locations on the same specimen.

4. Discussion

4.1. Surface residual stresses and their distribution

By substituting D', d, s and p listed in Table 2 into the stress model (Eqs. (A2a) and (A2b)), the stress distributions in both Al_2O_3 and Al_2O_3/SiC nanocomposites for the nominal plane

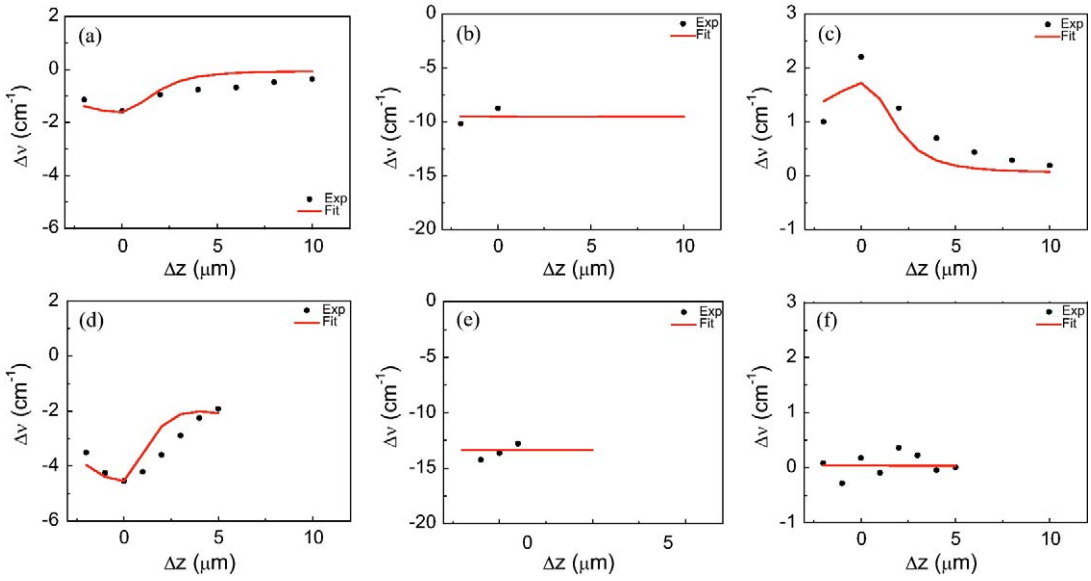

Fig. 7. Fitting results of Eqs. (A10–A12) to depth profiles of the ground alumina and 5 vol.% SiC nanocomposite. (a) peak shifts from the pullout, (b) broad peak shifts and (c) sharp-peak shifts from the ground surface of alumina; (d) peak shifts from the pullout, (e) broad peak shifts and (f) sharp-peak shifts from the ground surface of 5 vol.% SiC nanocomposite.

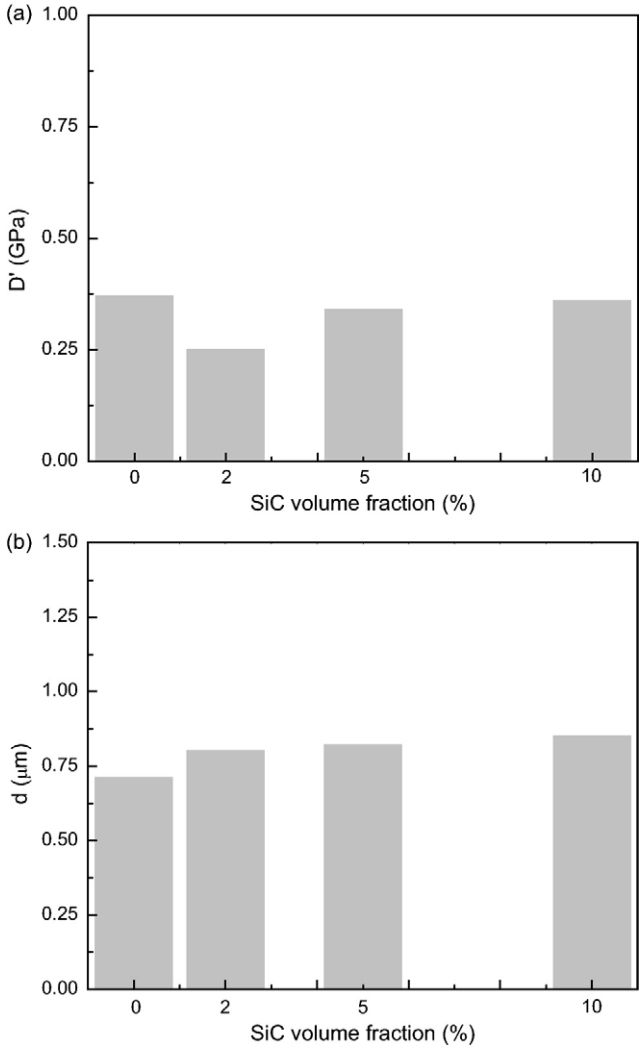

Fig. 8. Comparison between D' and d of Al_2O_3 and Al_2O_3/x vol.% SiC nanocomposites ($x = 2, 5, 10$).

strain stress state can be extracted from the model and are plotted in Fig. 9. Tensile σ_{xx} and σ_{zz} (the coordinates for the stress model are defined in Fig. A1) were present for some distance below the "ground" regions of the surface in alumina (in agreement with our previous work [25]) and the 2 vol.% SiC nanocomposite, but not in the 5 and 10 vol.% SiC nanocomposites. The maximum tensile stresses for σ_{xx} and σ_{zz} in the alumina and 2 vol.% SiC nanocomposite are ~1.25 GPa and ~350 MPa, and ~0.75 GPa and ~200 MPa, respectively (Table 3).

Caution has to be taken when considering the magnitude of the in-plane stresses (σ_{xx}) recalling the two-dimensional simplification of the grinding stress model (Section A.1). A plane strain state was assumed in the model where $\varepsilon_{yy} = 0$ and $\sigma_{yy} = \nu\sigma_{xx}$ at the surface. The true situation has biaxial symmetry in the surface plane and assuming the true in-plane stresses are $\sigma_{xx} = \sigma_{yy} = \sigma_t$, σ_t can be estimated by equalising the total normal stress that determines the peak shift in the two conditions: $2\sigma_t = (1+\nu)\sigma_{xx}$ and hence $\sigma_t = (1+\nu)\sigma_{xx}/2 = 0.62\sigma_{xx}$. It is thus evident that the stress model used in this work overestimates the in-plane stress by a factor of ~1.6 when fitted to the biaxial experimental results. The true values for the in-plane stresses, σ_t, estimated in this way, are also listed in Table 3. The out-of-plane stress σ_{zz} is expected to be affected less by this consideration as it arises from the sum of contributions in the notional grinding directions and so is insensitive to the relative contributions to the shift from the x and y directions.

Table 2 shows that D', which indicates the severity of plastic deformation in the plastically deformed layer, is similar between Al_2O_3 and Al_2O_3/SiC nanocomposites. The smaller stresses in alumina and 2 vol.% SiC nanocomposites compared to those in 5 and 10 vol.% SiC nanocomposites are due to the relaxation caused by greater amount of pullout. A simple demonstration of this is that comparison of the data in Tables 2 and 3 shows that the σ_{xx} values for the higher volume fraction nanocomposites are close to the pullout-free prediction of $-4\pi D'$, whereas the

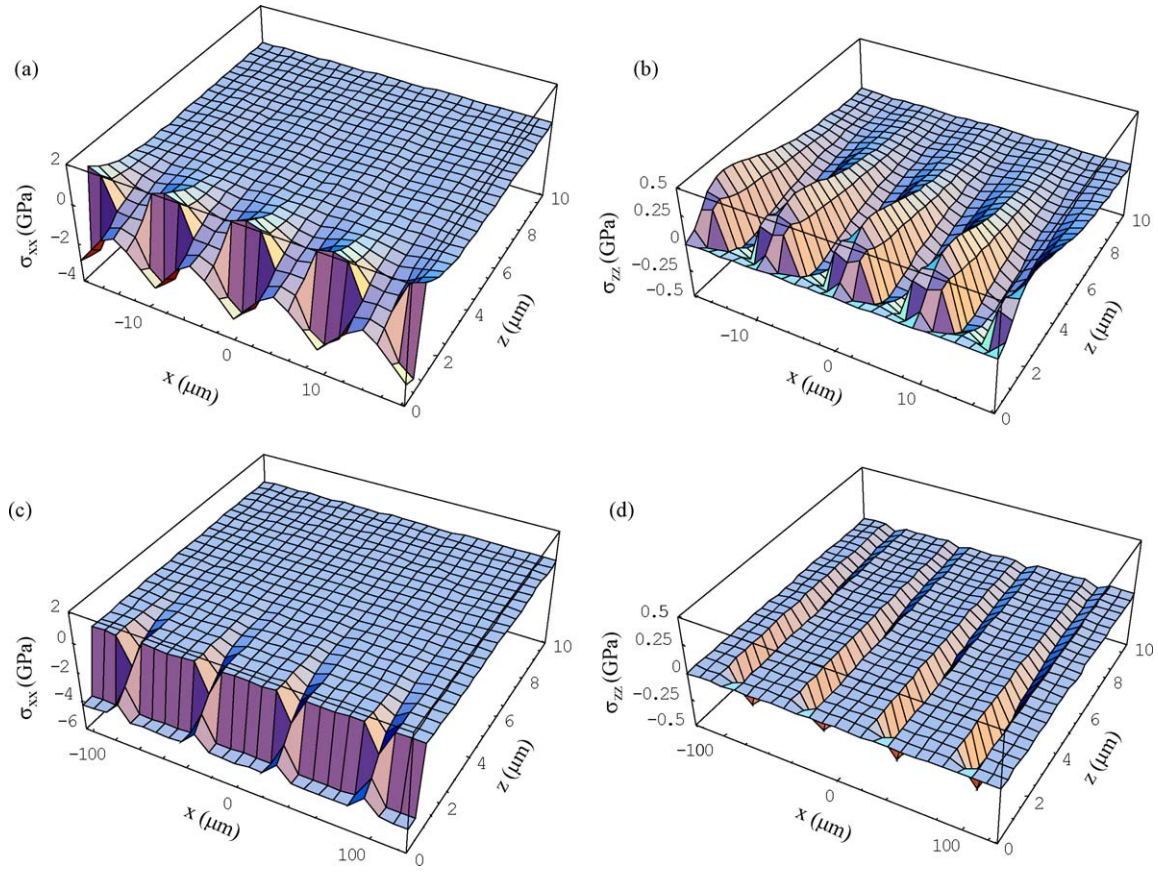

Fig. 9. Stress distributions in the ground alumina and 5 vol.% SiC nanocomposite. (a) σ_{xx} for alumina, (b) σ_{zz} for alumina, (c) σ_{xx} for 5 vol.% SiC nanocomposite and (d) σ_{zz} for 5 vol.% SiC nanocomposite. The surface is at $z=0$ and $x=0$ corresponds to the centre of a "ground" region of the surface. The σ_{xx} shown are based on the 2D model in Fig. A1.

stresses are considerably relaxed from this level for the alumina and the 2% SiC nanocomposite.

The depth of the plastic deformation, d, is also similar for the Al_2O_3 and the nanocomposites. This is in agreement with the results measured by high-resolution grazing-incidence parallel-beam X-ray powder diffraction ($d \approx 0.5\,\mu m$ for alumina and $\sim 0.4\,\mu m$ for 5 vol.% SiC nanocomposite) [17], but apparently different from results obtained using TEM [18], in which the depth to which twins and/or dislocations were observed in 150 μm grit ground Al_2O_3 and Al_2O_3/5 vol.% SiC nanocomposite was measured and assumed to be the thickness of the stressed layer. It was claimed in Ref. [18] that the depth of grinding damage in the nanocomposite (3–10 μm) is considerably larger than that in alumina (<1 μm), but the large uncertainty in determining the depth of damage in the nanocomposite was acknowledged. Although the difference between the results in Ref. [18] and in this work could be related to the more aggressive grinding condition in the former, it has to be pointed out that TEM is not ideal in determining the depth of the stressed surface layer: the defect density varies at different depths beneath the surface and is higher near the surface. Comparison of the present results with those in Ref. [18] suggests that the majority of the plastic deformation is concentrated near the surface and the dislocation activity observed in the nanocomposites at greater depths in Ref. [18] represents only a small amount of plastic strain.

Table 3
Maximum tensile and compressive stresses for ground regions and pullout regions for alumina and Al_2O_3/SiC nanocomposites as obtained by fitting the plane strain model in Fig. A1 to the experimental results. The in-plane stress estimates, σ_t, corrected to account for the biaxial in-plane stress state of the experiments are also listed.

Materials	Ground region ($x=0$)					Pullout region ($x=(s+p)/2$)		
	σ_{xx} ([a]t_{max}) (GPa)	σ_t ([a]t_{max}) (GPa)	σ_{xx} ([b]c_{max}) (GPa)	σ_t ([b]c_{max}) (GPa)	σ_{zz} (t_{max}) (GPa)	σ_{xx} (c_{max}) (GPa)	σ_t (c_{max}) (GPa)	σ_{zz} (c_{max}) (GPa)
Al_2O_3	1.26	0.78	−3.39	−2.10	0.34	−0.99	−0.61	−0.22
2 vol.% SiC	0.75	0.46	−2.39	−1.48	0.21	−1.09	−0.68	−0.21
5 vol.% SiC	0	0	−4.26	−2.64	0	−3.28	−2.03	−0.44
10 vol.% SiC	0	0	−4.52	−2.80	0	−3.70	−2.29	−0.47

[a] Maximum tensile stresses.
[b] Maximum compressive stresses.

The stress states in the materials beneath the pullouts are strongly compressive in both Al_2O_3 and Al_2O_3/SiC nanocomposites, and the maximum compressive stresses in 5 and 10 vol.% SiC nanocomposites are ~3.5 times and ~2 times those in alumina and 2 vol.% SiC nanocomposite, respectively, for σ_{xx} and σ_{zz} (Table 3). Considering the similar level of plastic deformation among them (D'), the difference is clearly a consequence of the greater area of unspalled, plastically deformed surface surrounding the pullouts in 5 and 10 vol.% SiC nanocomposites.

The compressive stresses obtained in this work are higher than those measured using other methods (ranging from ~50 MPa to 1.5 GPa) including curvature [15], X-ray diffraction [14,16,17] and Hertzian indentation [18,19]. The difference is believed to be mainly a consequence of the fact that the surface stresses measured in this work (Table 3) are peak stresses; the local variations in stress are taken into account rather than being volume averaged as in the other techniques.

4.2. Implications for surface finish and wear resistance

The evidence of tensile stresses is very important in explaining the cracking behaviour in grinding: tensile σ_{xx} will assist crack growth normal to the surface and tensile σ_{zz} will lead to material spalling off and grain pullout. Interestingly, tensile stresses are not present in the model before the pullout is introduced [21], neither are they present in 5 and 10 vol.% SiC nanocomposites and in polished polycrystalline alumina [25], where the amount of pullout is small (Table 1). Two conclusions can be drawn from this. First, once pullouts start to form by surface fracture, it becomes easier to form further pullouts owing to the increasingly tensile stresses parallel to and normal to the surface just beneath the plastically deformed layer. This positive feedback leads to instability and can possibly account for the sudden and catastrophic transition from mild to severe wear that is often observed after some time in sliding wear tests. Second, the initial resistance to fracture and pullout during grinding of Al_2O_3/SiC nanocomposites with more than 5 vol.% nano-sized SiC addition prevents the development of tensile stresses that could aid such processes subsequently. This makes the grinding of 5 and 10 vol.% SiC nanocomposites a more stable process compared to that of alumina and 2 vol.% SiC nanocomposite and the amount of pullout remains small. This provides a convincing explanation for the exceptional resistance of the nanocomposites to this mild to severe transition compared with alumina that has been reported experimentally [36].

The initial much smaller amount of pullout in 5 and 10 vol.% SiC nanocomposites is because the large amount of nano-sized SiC addition can effectively suppress crack initiation [33,36]. The improved surface quality of 5 and 10 vol.% SiC nanocomposites compared to alumina and 2 vol.% SiC nanocomposite is therefore due to the combined effect of both suppression of initial crack formation and the consequent suppression of tensile residual stresses later in the grinding process.

4.3. Implications for strength

The resistance of the nanocomposites to surface cracking initiation [9,13,18] gives an obvious reason for their high strength. The results in Table 3 show two additional reasons for ground nanocomposites containing 5 vol% SiC or more to be stronger than ground specimens of alumina and more dilute nanocomposites. Firstly, the 5 and 10 vol% SiC nanocomposites contain higher compressive surface stresses, inhibiting surface crack propagation. Secondly, the compressive stresses in these materials are uniform and they contain almost no tensile residual stresses, whereas the alumina and 2% SiC nanocomposites contain regions in which there are strong tensile stresses parallel to the surface that can actually help cracks to propagate, negating the effect of the compressive regions.

It should be noted, however, that these results indicate that residual stresses would give little improvement in strength for the nanocomposites compared with alumina when well polished specimens are used because there is little surface fracture and pullout in any material under these conditions. In this case, the similarity in plastic response of the materials (D' and d) indicates that any surface stresses would also be similar. The higher strength of the nanocomposites in such cases must therefore result from the better resistance to crack initiation and improved toughness owing to the change in fracture mode on adding SiC.

5. Summary

High spatial resolution measurements of surface residual stresses in ground surfaces of Al_2O_3 and Al_2O_3/x vol.% SiC nanocomposites ($x = 2, 5, 10$) were made by Cr^{3+} fluorescence microspectroscopy. In order to allow correctly for the translucency of the materials in interpreting the results, the probe response function was measured for the different materials and convoluted with the predictions of a model for the grinding stresses. The surfaces of the Al_2O_3 and 2 vol.% SiC nanocomposite exhibited considerable surface fracture and pullout. The surface residual stresses in these materials were highly inhomogeneous. In-plane stresses ranged from ~ −2 GPa (compressive) within plastically deformed surface layers of the surface to ~ +0.8 GPa (tensile) immediately beneath them. Out of plane tensile stresses ~ 0.2–0.3 GPa were present beneath the deformed surface layers. Nanocomposites containing 5 and 10 vol.% SiC exhibited little surface fracture and pullout. The stresses were much more homogeneous with negligible tensile stress either in-plane or out of plane. Instead, the surface stress state consisted of a very high, almost uniform compressive in-plane stress of ~ −2.7 GPa within the plastically deformed surface layer.

The extent of plastic deformation within the surface layer was similar in all the materials as was the effective depth of plastic deformation (0.7–0.85 μm); the differences in stress level and homogeneity were solely a consequence of the different amounts of surface fracture and pullout.

The results show that the reduction in surface pullout in nanocomposites containing 5 vol.% SiC or more also leads to the suppression of further surface crack propagation and pullout; conversely, the initial surface fracture and pullout in Al_2O_3 and dilute nanocomposites helps to produce further surface fracture. The stability of surface fracture in the nanocomposites helps to explain their higher strength and resistance to severe wear.

Acknowledgements

S. Guo would like to thank the K C Wong Education Foundation and the Overseas Research Students Awards Scheme, and A. Limpichaipanit would like to thank the Thai government, for financial support of their D.Phil study in the University of Oxford.

Appendix A.

A.1. Model for grinding stresses

Fig. A1 shows the geometry of the grinding stress model. The ground surface is on the *xy* plane. The grinding process generates a compressed layer at the surface due to plastic deformation [18]. This is simulated in the "ground" regions of the model by continuously distributed edge dislocations with their Burgers vectors parallel to the *x* axis, line direction parallel to *y* and located at depth *d* below the surface, corresponding to the depth of plastic deformation. These are fictitious dislocations whose presence is simply to model the overall deformation of the plastically deformed layer; they do not represent the real dislocations formed during grinding. The extent of plastic deformation, and therefore the density of fictitious dislocations at the bottom of the ground layer is assumed to be uniform. It should be noted here that the model based on Fig. A1 is essentially two dimensional (plane strain), corresponding to unidirectional grinding damage, while the condition in the experiments is a three-dimensional case because the specimen rotates relative to the grinding wheel during machining. This simplified treatment can reasonably account for the main features of the experimental results but the as-obtained in-plane stresses (σ_{xx}) are overestimated. This is further discussed in Section 4.1.

Pullouts are represented in the model by dislocation-free regions on the assumption that the material removed in a pullout comes from a depth sufficient to remove the entire plastically deformed layer at that point. This is supported by the absence of an extra "broad" doublet in spectra from the pullouts (e.g. Fig. 4(a) inset with two peak fit) indicating the absence of a significant amount of plastically deformed material. In reality, a pullout corresponds to a cavity in the surface (Fig. A1(b)), but in the model the surface is flat, even at the pullouts (Fig. A1(a)), to facilitate solution of the stress problem. To simplify the problem further all the pullouts and islands of ground surface have constant breadths, *p* and *s*, respectively. The origin of the coordinate system is set at the surface, in the middle of a "ground" region of the surface.

The elastic stresses in the model of Fig. A1(a) have been derived previously [25]. The starting point is the stress field of a single edge dislocation located at (0, *d*). The normal stress components in the *x*-*z* plane are:

$$\sigma_{xx}(x,z) = DF(x,z,d) = D\left[\frac{(z-d)[3x^2+(z-d)^2]}{[x^2+(z-d)^2]^2} + \frac{-d[x^4-(z+d)(d^3+(d^2+6x^2)z-dz^2-z^3)]}{[x^2+(z+d)^2]^3} + \frac{[-4dx^2(d^2+x^2)-3(d^2+x^2)^2z-2d(5d^2+3x^2)z^2-4(3d^2+x^2)z^3-6dz^4-z^5]}{[x^2+(z+d)^2]^3}\right] \quad \text{(A1a)}$$

$$\sigma_{zz}(x,z) = DG(x,z) = D\left[\frac{-(z-d)[x^2-(z-d)^2]}{[x^2+(z-d)^2]^2} + \frac{d[-x^4+(z+d)(d^3+5d^2z-6x^2z+7dz^2+3z^3)]}{[x^2+(z+d)^2]^3} + \frac{z[d^4-6d^2x^2+x^4+2d^3z-z^4-2d(3x^2z+z^3)]}{[x^2+(z+d)^2]^3}\right] \quad \text{(A1b)}$$

where $D = \mu b/2\pi(1-\nu)$, μ is the shear modulus, b the magnitude of the Burgers vector, and ν is Poisson's ratio, taken to be 0.24 in this work.

Summing the contributions from all the continuously distributed dislocations located at $z=d$ the normal stress components at any position (x, z) in the model of Fig. A1(a) are:

$$\sigma_{xx}(x,z) = D'\left[\int_{-s/2}^{+s/2} F(x-x_q,z,d)dx_q + \int_{s/2+p}^{3s/2+p} F(x-x_q,z,d)dx_q + \int_{-(3s/2+p)}^{-(s/2+p)} F(x-x_q,z,d)dx_q + \int_{3s/2+2p}^{5s/2+2p} F(x-x_q,z,d)dx_q\right]$$

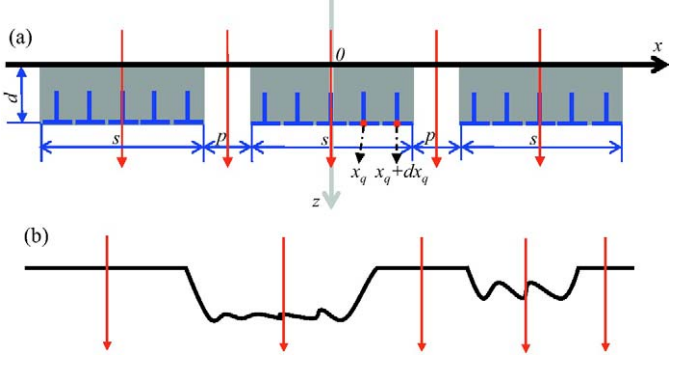

Fig. A1. (a) Schematic of islands of ground or polished surface (average size: *s*) and pullouts (average size: *p*) in the stress model. The distance between two neighbouring dislocations, dx_q, is exaggerated for clarity. The arrows across the centres of the pullout and islands of the ground/polished surface indicate the depth scan path. (b) Schematic of the real ground/polished surface and pullouts where the rough surface of the pullout and the varying size of islands of ground/polished surface and pullouts are indicated.

$$+\int_{-(5s/2+2p)}^{-(3s/2+2p)} F(x-x_q,z,d)dx_q+\cdots$$
$$+\int_{(2n-3)s/2+(n-1)p}^{(2n-1)s/2+(n-1)p} F(x-x_q,z,d)dx_q$$
$$+\int_{-[(2n-1)s/2+(n-1)p]}^{-[(2n-3)s/2+(n-1)p]} F(x-x_q,z,d)dx_q\Bigg](1\le n<\infty) \quad \text{(A2a)}$$

$$\sigma_{zz}(x,z) = D'\left[\int_{-s/2}^{+s/2} G(x-x_q,z,d)dx_q\right.$$
$$+\int_{s/2+p}^{3s/2+p} G(x-x_q,z,d)dx_q$$
$$+\int_{-(3s/2+p)}^{-(s/2+p)} G(x-x_q,z,d)dx_q$$
$$+\int_{3s/2+2p}^{5s/2+2p} G(x-x_q,z,d)dx_q$$
$$+\int_{-(5s/2+2p)}^{-(3s/2+2p)} G(x-x_q,z,d)dx_q+\cdots$$
$$+\int_{(2n-3)s/2+(n-1)p}^{(2n-1)s/2+(n-1)p} G(x-x_q,z,d)dx_q$$
$$+\int_{-[(2n-1)s/2+(n-1)p]}^{-[(2n-3)s/2+(n-1)p]} G(x-x_q,z,d)dx_q\Bigg](1\le n<\infty) \quad \text{(A2b)}$$

where n is the number of pullouts, x_q is an integration variable shown in Fig. A1(a) and $D'=\mu b'/2\pi(1-\nu)$, in which b' is the Burgers vector of continuously distributed dislocation per unit distance in the x direction. b' and therefore D' are measures of the extent to which the "ground" layer has been plastically deformed; the in-plane stress σ_{xx} predicted by this plane strain model in the absence of pullout is $-4\pi D'$ [21].

A plane strain state is assumed and hence:

$$\sigma_{yy}=\nu(\sigma_{xx}+\sigma_{zz}) \quad \text{(A3)}$$

$$\sigma_{xx}+\sigma_{yy}+\sigma_{zz}=(1+\nu)(\sigma_{xx}+\sigma_{zz}) \quad \text{(A4)}$$

The predicted stress at a point is converted to a Cr^{3+} fluorescence peak shift through Eq. (1). For a randomly orientated, fine grained polycrystal subjected to a uniform stress, Eq. (1) has the simplified form [37]:

$$\Delta\nu(x,z)=\frac{\Pi_{11}+\Pi_{22}+\Pi_{33}}{3}(\sigma_{11}+\sigma_{22}+\sigma_{33})$$
$$=\frac{\Pi_{11}+\Pi_{22}+\Pi_{33}}{3}(\sigma_{11}+\sigma_{22}+\sigma_{33})$$
$$=3.14(\sigma_{xx}+\sigma_{zz}) \quad \text{(A5)}$$

when averaged over grains of all orientations, with $\Pi_{11}=2.56\,\mathrm{cm^{-1}\,GPa^{-1}}$, $\Pi_{22}=3.50\,\mathrm{cm^{-1}\,GPa^{-1}}$, and $\Pi_{33}=1.53\,\mathrm{cm^{-1}\,GPa^{-1}}$ [30].

The depth scans through the "ground" surface regions were assumed to pass through the centres of the islands (Fig. A1), so the predicted peak shift in the depth profile across the ground surface is expressed as $\Delta\nu(0,z)$. This mirrors the experiments, and in any case it is shown in Section 4.1 that the stress variation with x is slow at the centre of a "ground" region. Similarly, the predicted peak shift for the depth profile measurements through the pullouts can be expressed as $\Delta\nu\left(\frac{s+p}{2},z\right)$.

The integrals in Eqs. (A2a) and (A2b) were carried out numerically using the commercial software package, Mathematica (Wolfram Research, USA). $n=100$ was used and it was shown that further increase of n had a negligible effect on the results.

A.2. Probe response function (PRF)

When the laser is focused at a distance z_0 ($z_0=n'\Delta z$, where n' is the effective refractive index [22,38]) below the surface of a translucent material, the signal generated in a finite volume of material is collected (Fig. 6). The total signal collected at depth z_0 is the integral of the fluorescence from all depths within the material [26]:

$$I(z_0)=\int_0^t g(z,z_0)dz \quad \text{(A6)}$$

where t is the thickness of material (t can be assumed to be infinite because of the absorption that limits the probeable length) and $g(z,z_0)$ is the PRF.

If allowance is made for refraction, Eq. (A6) can be written as a function of sample surface displacement relative to the focal plane, Δz:

$$I(\Delta z)=\int_0^t g(z,\Delta z)dz \quad \text{(A7)}$$

A suitable depth resolution function, $g(z,\Delta z)$, for the present combination of instrument and material is already known from our previous work [22] and is given in Eq. (A8). It captures all relevant physical effects including refraction, absorption and scattering by pores and grain boundaries.

$$g(z,\Delta z)=e^{-2\alpha}\left[A_1\frac{w_1}{{w_1}^2+(z-n'\Delta z)^2}+A_2\frac{w_2}{{w_2}^2+(z-n'\Delta z)^2}\right] \quad \text{(A8)}$$

where α is the absorption coefficient; n' is the effective refractive index [22,38]; w_1 is the probe length of the microscope and w_2 is the virtual probe length proposed to account for scattering by pores etc.; A_1 and A_2 represent the relative contributions from unscattered and scattered radiation to the collected intensity. The measured parameters in Eq. (A8) appropriate for Al_2O_3 and Al_2O_3/SiC nanocomposites [22] are given in Table A1. The values of the absorption coefficient, α, in the table show that the nanocomposites are significantly less translucent than the alumina.

Table A1
List of parameters in Eq. (A8) for Al_2O_3 and Al_2O_3/SiC nanocomposites.

Material	α (μm^{-1})	w_1 (μm)	w_2 (μm)	A_1	A_2	A_2/A_1
Al_2O_3	0.0403	2.88	71.6	0.605	0.221	0.365
2 vol.% SiC	0.104	2.88	36.2	0.890	0.560	0.629
5 vol.% SiC	0.143	2.88	29.5	0.955	1.809	1.89
10 vol.% SiC	0.305	2.88	16.1	1.29	3.34	2.59

A.3. Convolution and fitting to experimental depth scans

Supposing the stress field is a function of depth only, which is reasonable in this case because the depth resolution is lower than the lateral resolution and because the results of the modelling show that the variation of stress with x is slow at the centre of a pullout or ground region [21], the experimentally measured peak shift at depth Δz is a weighted average of the signals from all depths [26]:

$$\overline{\Delta\nu(\Delta z)} = \frac{\int_0^t \Delta\nu(z)g(z,\Delta z)dz}{\int_0^t g(z,\Delta z)dz} \tag{A9}$$

where $\Delta\nu(z)$ is the real peak shift at any depth and $\overline{\Delta\nu(\Delta z)}$ is the weighted average peak shift at depth Δz, which is also the experimentally measured R-line shift.

The R1 fluorescence peaks shifts predicted by the model may be obtained by the convolution in Eq. (A9) over appropriate limits. There are three cases. For the broad peaks corresponding to the stress state within the plastically deformed surface layer in "ground" regions, the peak shift during a depth scan is given by:

$$\overline{\Delta\nu(\Delta z)} = \frac{\int_0^d \Delta\nu(0,z)g(z,\Delta z)dz}{\int_0^d g(z,\Delta z)dz} \tag{A10}$$

For the sharp peaks in "ground" regions the convolution is:

$$\overline{\Delta\nu(\Delta z)} = \frac{\int_d^t \Delta\nu(0,z)g(z,\Delta z)dz}{\int_d^t g(z,\Delta z)dz} \tag{A11}$$

Similarly, for the depth profiles through the pullouts, the predicted peak shift follows:

$$\overline{\Delta\nu(\Delta z)} = \frac{\int_0^t \Delta\nu\left(\frac{s+p}{2},z\right)g(z,\Delta z)dz}{\int_0^t g(z,\Delta z)dz} \tag{A12}$$

In our previous work [25], fittings to the experimental results were based on the broad peak and sharp peak shifts from the depth profiles through the "ground" regions of the surfaces only (Eqs. (A10) and (A11)). However, for 5 and 10 vol.% SiC nanocomposites, the sharp-peak shifts are small and hence difficult to fit. To achieve a consistent comparison, all the fittings in this work were based on the broad peak shifts from the depth profiles through ground surfaces and depth profiles through the pullouts using Eqs. (A10) and (A12). The experimentally measured values of s and p were used, and D' and d were varied to reach a compromise best fit for both cases. Only results with the focal plane at or beneath the surface were used; when the focal plane is above the surface, the signal obtained comes from one of the tails of the PRF and this is not accurately modelled by Eq. (A8). The fitted values of D' and d were then used to predict the sharp peak shifts from depth profiles through the "ground" regions of surface, with no further adjustment of parameters.

References

[1]. Nakahira A, Niihara K. Sintering behaviors and consolidation process for Al_2O_3/SiC nanocomposites. *Journal of the Ceramic Society of Japan* 1992;**100**:448.

[2]. Niihara K. New design concept of structural ceramics. Ceramic nanocomposites. *Journal of the Ceramic Society of Japan* 1991;**99**:974.

[3]. Niihara K, Nakahira A. Strengthening and toughening mechanisms in nanocomposite ceramics. *Annales De Chimie-Science Des Materiaux* 1991;**16**:479.

[4]. Carroll L, Sternitzke M, Derby B. Silicon carbide particle size effects in alumina-based nanocomposites. *Acta Materialia* 1996;**44**:4543.

[5]. Borsa CE, Jiao S, Todd RI, Brook RJ. Processing and properties of Al_2O_3/SiC nanocomposites. *Journal of Microscopy-Oxford* 1995;**177**:305.

[6]. Stearns L, Zhao J, Harmer MP. Processing and microstructure development in Al_2O_3–SiC nanocomposites. *Journal of the European Ceramic Society* 1992;**10**:473.

[7]. Sternitzke M, Derby B, Brook RJ. Alumina/silicon carbide nanocomposites by hybrid polymer/powder processing: microstructures and mechanical properties. *Journal of the American Ceramic Society* 1998;**81**:41.

[8]. Davidge RW, Brook RJ, Cambier F, Poorteman M, Leriche A, O'Sullivan D, et al. Fabrication, properties, and modelling of engineering ceramics reinforced with nanoparticles of silicon carbide. *British Ceramic Transactions* 1997;**96**:121.

[9]. Zhao J, Stearns LC, Harmer MP, Chan HM, Miller GA. Mechanical behavior of alumina–silicon carbide nanocomposites. *Journal of the American Ceramic Society* 1993;**76**:503.

[10]. Walker CN, Borsa CE, Todd RI, Davidge RW, Brook RJ. Fabrication, characterisation and properties of alumina matrix nanocomposites. *British Ceramic Proceedings Series* 1995;**53**:249.

[11]. Rodriguez J, Martin A, Pastor JY, Llorca J, Bartolome JF, Moya JS. Sliding wear of alumina/silicon carbide nanocomposites. *Journal of the American Ceramic Society* 1999;**82**:2252.

[12]. Ortiz-Merino JL, Todd RI. Relationship between wear rate, surface pullout and microstructure during abrasive wear of alumina and alumina/SiC nanocomposites. *Acta Materialia* 2005;**53**:3345.

[13]. Limpichaipanit A, Todd RI. The relationship between microstructure, fracture and abrasive wear in Al_2O_3/SiC nanocomposites and microcomposites containing 5 and 10% SiC. *Journal of the European Ceramic Society* 2009;**29**:2841.

[14]. Tanner BK, Wu HZ, Roberts SG. Direct evidence for compressive elastic strain at ground surfaces of nanocomposite ceramics. *Applied Physics Letters* 2005:86.

[15]. Chou IA, Chan HM, Harmer MP. Machining-induced surface residual stress behavior in Al_2O_3–SiC nanocomposites. *Journal of the American Ceramic Society* 1996;**79**:2403.

[16]. Lange FF, James MR, Green DJ. Determination of residual surface stresses caused by grinding in polycrystalline Al_2O_3. *Journal of the American Ceramic Society* 1983;**66**:C16.

[17]. Tanner BK, Wu HZ, Roberts SG, Hase TPA. Subsurface damage in alumina and alumina-silicon carbide nanocomposites. *Philosophical Magazine* 2004;**84**:1219.

[18]. Wu H, Roberts SG, Derby B. Residual stress and subsurface damage in machined alumina and alumina/silicon carbide nanocomposite ceramics. *Acta Materialia* 2001;**49**:507.

[19]. Wu HZ, Lawrence CW, Roberts SG, Derby B. The strength of Al_2O_3/SiC nanocomposites after grinding and annealing. *Acta Materialia* 1998;**46**:3839.

[20]. Withers PJ, Turski M, Edwards L, Bouchard PJ, Buttle DJ. Recent advances in residual stress measurement. *International Journal of Pressure Vessels and Piping* 2008;**85**:118.

[21]. Guo, S. *Fluorescence microscopy investigation on residual stresses in alumina-based ceramics*. Ph.D. thesis. University of Oxford; 2009.
[22]. Guo S, Todd RI. Confocal fluorescence microscopy in alumina-based ceramics: where does the signal come from? *Journal of the European Ceramic Society* 2010;**30**:641.
[23]. Molis SE, Clarke DR. Measurement of stresses using fluorescence in an optical microprobe: stresses around indentations in a chromium-doped sapphire. *Journal of the American Ceramic Society* 1990;**73**:3189.
[24]. Wu HZ, Roberts SG, Derby B. Residual stress distributions around indentations and scratches in polycrystalline Al_2O_3 and Al_2O_3/SiC nanocomposites measured using fluorescence probes. *Acta Materialia* 2008;**56**:140.
[25]. Guo S, Todd RI. Cr3+ microspectroscopy measurements and modeling of local variations in surface grinding stresses in polycrystalline alumina. *Journal of European Ceramic Society* 2010;**30**:2533.
[26]. Ma Q, Clarke DR. Measurement of residual stresses in sapphire fiber composites using optical fluorescence. *Acta Metallurgica et Materialia* 1993;**41**:1817.
[27]. Wurst JC, Nelson JA. Linear intercept technique for measuring grain-size in a 2-phase polycrystalline ceramics. *Journal of the American Ceramic Society* 1972;**55**:109.
[28]. Ma Q, Clarke DR. Optical fluorescence from chromium ions in sapphire – a probe of the image stress. *Acta Metallurgica et Materialia* 1993;**41**:1811.
[29]. Grabner L. Spectroscopic technique for measurement of residual-stress in sintered Al_2O_3. *Journal of Applied Physics* 1978;**49**:580.
[30]. He J, Clarke DR. Determination of the piezospectroscopic coefficients for chromium-doped sapphire. *Journal of the American Ceramic Society* 1995;**78**:1347.
[31]. He J, Clarke DR. Polarization dependence of the Cr^{3+} R-line fluorescence from sapphire and its application to crystal orientation and piezospectroscopic measurement. *Journal of the American Ceramic Society* 1997;**80**:69.
[32]. Eggert JH, Goettel KA, Silvera IF. Ruby at high pressure. 1. Optical line shifts to 156 GPa. *Physical Review B* 1989;**40**:5724.
[33]. Todd RI, Limpichaipanit A. Microstructure–property relationships in wear resistant alumina/SiC nanocomposites. *Advances in Science and Technology* 2006;**45**:555.
[34]. Winn AJ, Todd RI. Microstructural requirements for alumina–SiC nanocomposites. *British Ceramic Transactions* 1999;**98**:219.
[35]. Munro RG, Piermarini GJ, Block S, Holzapfel WB. Model line-shape analysis for the ruby R lines used for pressure measurement. *Journal of Applied Physics* 1985;**57**:165.
[36]. Wu H, Inkson BJ, Roberts SG. Subsurface deformation of machined Al_2O_3 and Al_2O_3/5vol%SiC nanocomposite. *Journal of Microscopy-Oxford* 2001;**201**:212.
[37]. Ma Q, Clarke DR. Stress measurement in single-crystal and polycrystalline ceramics using their optical fluorescence. *Journal of the American Ceramic Society* 1993;**76**:1433.
[38]. Everall NJ. Modeling and measuring the effect of refraction on the depth resolution of confocal Raman microscopy. *Applied Spectroscopy* 2000;**54**:773.